



Functional optical coherence tomography and photoacoustic microscopy imaging for zebrafish larvae

RICHARD HAINDL,^{1,*}  ABIGAIL J. DELORIA,¹ CATERINA STURTZEL,² HARALD SATTMANN,¹ WOLFGANG ROHRINGER,³ BALTHASAR FISCHER,³ MARCO ANDREANA,¹  ANGELIKA UNTERHUBER,¹  THORSTEN SCHWERTE,⁴ MARTIN DISTEL,² WOLFGANG DREXLER,¹ RAINER LEITGEB,¹ AND MENGYANG LIU¹ 

¹Center for Medical Physics and Biomedical Engineering, Medical University of Vienna, Vienna, Austria

²Innovative Cancer Models, St. Anna Children's Cancer Research Institute, Vienna, Austria

³XARION Laser Acoustics GmbH, Vienna, Austria

⁴Institute of Zoology, University of Innsbruck, Innsbruck, Austria

*richard.haindl@meduniwien.ac.at

Abstract: We present a dual modality functional optical coherence tomography and photoacoustic microscopy (OCT-PAM) system. The photoacoustic modality employs an akinetic optical sensor with a large imaging window. This imaging window enables direct reflection mode operation, and a seamless integration of optical coherence tomography (OCT) as a second imaging modality. Functional extensions to the OCT-PAM system include Doppler OCT (DOCT) and spectroscopic PAM (sPAM). This functional and non-invasive imaging system is applied to image zebrafish larvae, demonstrating its capability to extract both morphological and hemodynamic parameters *in vivo* in small animals, which are essential and critical in preclinical imaging for physiological, pathophysiological and drug response studies.

© 2020 Optical Society of America under the terms of the [OSA Open Access Publishing Agreement](#)

1. Introduction

The zebrafish, *Danio rerio*, is a freshwater fish originally used as a vertebrate animal model to study molecular genetics and developmental biology [1,2]. The zebrafish and in particular zebrafish larvae provide several advantages and complementing features to other common model organisms like *C. elegans*, *Drosophila* or mice. The small body size, optical transparency, fecundity, *ex utero* development and the independence of convective oxygen transport in stages before 8 days post fertilization (dpf) make zebrafish larvae a well-suited model for experimental and genetic studies of organogenesis [3–5]. Despite some differences like the lack of lungs, many other organ systems including the cardiovascular, the nervous and the hematopoietic systems are conserved in function and development between zebrafish and humans [6].

In vivo analysis of vascular development in zebrafish larvae is primarily based on confocal microscopy and the use of transgenic zebrafish strains. Highlighting vascular endothelial cells by fluorescent protein expression, like *tg(fli1a:EGFP)^{y1}* or microangiography based on the injection of labeled particles including quantum dots into circulation [7–10] is common. However, the introduction of an exogenous label always bears the risk of perturbing the process under investigation. Furthermore, studying the interplay of several cell types or structures, simultaneous investigation is limited by the number of fluorophores with non-overlapping spectra. In addition, the shallow imaging depth of confocal microscopy and the lack of functional parameters that can be retrieved by current methods require a better tool for zebrafish larval imaging. The ideal imaging method of choice would be non-invasive, relies on the intrinsic contrast of the sample and be able to provide functional parameters like blood flow and oxygenation level. Considering the

optical transparency of zebrafish larvae and the availability of various endogenous chromophores such as melanin and hemoglobin, modern non-invasive 3-D optical imaging modalities such as photoacoustic microscopy (PAM) [11,12] and optical coherence tomography (OCT) [13,14] are potential successors to traditional methods imaging the zebrafish larva.

PAM's contrast originates from light absorbing chromophores [11,12]. For pigment suppressed zebrafish larvae, PAM visualizes the cardiovascular system of the fish, since hemoglobin is the major absorber [15,16]. Light absorption in most of the larva's tissue is weak for typical PAM excitation wavelengths. Therefore, no information or contrast on the zebrafish morphology can be extracted by relying on PAM as the only imaging modality.

To provide morphological contrast, other imaging modalities can be combined with PAM as has been demonstrated for mouse ear and retinal imaging before [17–22]. Zebrafish larval imaging, however, is delicate and necessitates a careful selection of transducer technologies and sophisticated system alignment. Previously, a photoacoustic, confocal, and two-photon microscopy system demonstrated to have the capability of imaging the spinal cord, posterior lateral line and vasculature of zebrafish [23]. Multi-photon, as well as brightfield, second and third harmonic generation microscopy has been combined with PAM to image melanin and muscle fibrils in the zebrafish larva [23,24]. Recently, efforts have been made to combine PAM and photoacoustic radiometry with fluorescence imaging to image transgenic zebrafish larvae *in vivo* [25,26], where photoacoustic radiometry measures the light extinction coefficient and gives morphological contrast of the gross anatomy based on tissue light extinction.

While promising, the PAM modality in current multimodal systems for zebrafish larval imaging suffers from slow imaging speed and low signal intensities. These drawbacks necessitate very long imaging sessions and heavy signal averaging, i.e. complicating the capture of moving cells in living animals [16,25]. The use of a focused piezoelectric transducer in transmission mode operation with a water tank as acoustic couplant further complicates the integration of other imaging modalities [15,16,24,25]. Finally, the multimodal systems reviewed above combine an intrinsic 3-D imaging modality (PAM) with a quasi 2-D imaging modality (confocal, two-photon, fluorescence imaging and photoacoustic radiometry) [23–27], which debilitates the value of multimodality.

Recently a multimodal optical coherence tomography and photoacoustic microscopy system (OCT-PAM) was introduced [28]. The system uses an optical akinetic sensor [29], which can be positioned on top of the sample for reflection mode imaging. Zebrafish larva's tissue and vascular morphologies are resolved by OCT and PAM, respectively by this system in 3-D. However, this reflection mode OCT-PAM system is still limited in speed due to the use of stepper motors for scanning and the need of signal averaging. The superluminescent diode (SLED) light source used for OCT in that system combines three SLEDs, which are not polarization aligned, causing various artifacts and reduced axial resolution in a fiber based system [30].

Hereby we demonstrate the capabilities of an ultra-high resolution OCT-PAM system which not only overcomes the limitations of previous and classical imaging systems, but also brings functional measuring capabilities. Fast laser scanning reduces the imaging time to a few minutes for a full body OCT-PAM scan of the whole zebrafish larva. A Ti:Sapphire based broad bandwidth laser enhances the axial resolution of the OCT subsystem to 2.4 μm , enabling unprecedented visualization of organs and retinal layers with OCT *in vivo*. The implementation of Doppler OCT (DOCT) and spectroscopic PAM (sPAM) allows us to monitor arterial pulsation, calculate absolute blood flow, oxygen saturation and oxygen distribution on a microscopic level in the body and eye of the zebrafish larva. Our work demonstrates, for the first time, the superior capabilities of OCT-PAM for future morphological, pathophysiological and drug response studies in a vertebrate model organism [5,6,31–35].

2. Methods

The schematic of the functional OCT-PAM system can be found in Fig. 1. For PAM an akinetic optical sensor with a large imaging window (2 mm · 12 mm) is used to detect refractive index modulations caused by acoustic waves [28,29]. The implementation of the detector allows direct reflection mode imaging, making it suitable for easy integration of OCT.

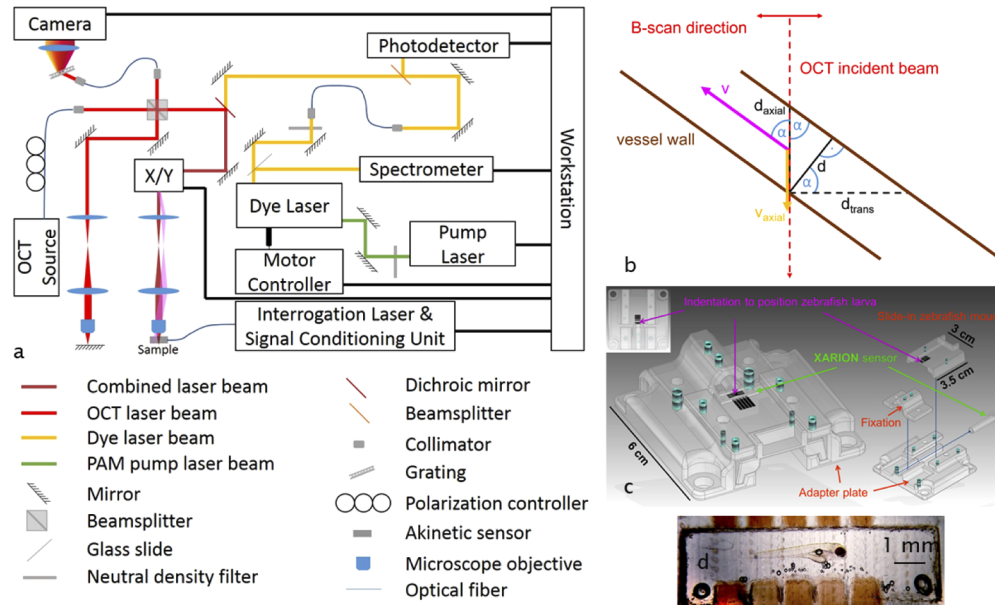


Fig. 1. (a) Functional OCT-PAM system. (b) Absolute velocity extraction principle for zebrafish body and eye. (c) 3-D printed zebrafish larva mount. (d) Zebrafish larva in recovery position mounted in the indentation of the zebrafish mount.

The bulk optics (90:10 beamsplitter) Michelson interferometer based spectral domain OCT sub-system features a Ti:Sapphire laser (150 nm) centered at 780 nm for ultra-high resolution OCT imaging. The homemade spectrometer consists of a transmission grating with 1200 lines/mm (3253-W-01, Wasatch Photonics), a focusing lens (85 mm f/2.0 Makro-Planar T, Zeiss), and a line scan camera (Sprint spl4096, Basler), where 2500 pixel are used for read-out.

The photoacoustic excitation source (SPOT-10-100-532, Elforlight) generates either 532 nm pulses at 50 kHz pulse repetition rate or tunable wavelengths between 560 nm to 590 nm through a dye laser (DL-10-5, Elforlight) at 10 kHz using laser grade highly purified dye (Pyromethene P597, Exciton) dissolved in Ethanol (Ethanol absolute, VWR Chemicals). The excitation laser light is coupled into a 1 m single mode fiber (P1-460P-FC-1, Thorlabs), which guides the coupled light to the scanner, where OCT and PAM sub-systems are combined by a dichroic shortpass mirror (69-205, Edmund Optics).

The sample arm of the imaging system comprises a pair of galvanometer scanning mirrors (CTI6220H, Cambridge Technology), a 4f lens system (AC254-050-B-ML and AC254-075-B, Thorlabs) and a microscope objective (UPlanSApo 4, Olympus) to perform raster scanning across the sample. The collimated beam has a beam width of 8 mm after the collimator (RC08APC-P01, Thorlabs). This width is expanded to 12 mm to fill the aperture of the objective (NA = 0.16). The same optical elements are used in the reference arm to minimize dispersion in OCT. A summary of the system specifications is given in Tab. 1.

Table 1. System specifications

OCT		PAM	
Parameters	Specifications	Parameters	Specifications
Light source	broadband Ti:Sapphire laser	Light source	Elforlight pump, dye laser
Center wavelength $\bar{\lambda}$	780 nm	Wavelength	532 nm, 560 nm to 590 nm
Bandwidth $\Delta\lambda$	150 nm	Line and pulse width	3 nm, 2 ns (pulsed)
Power on the sample	2 mW	Pulse energy on the sample	80 nJ
typical A-scan rate	10 kHz (up to 140 kHz)	Repetition rate	50 kHz, 10 kHz
Signal to noise ratio	98 dB (measured at 60 kHz)	Noise-equivalent pressure	$530 \mu\text{Pa}/\sqrt{\text{Hz}}$
Axial resolution (tissue)	2.4 μm	Axial resolution	286 μm
Transverse resolution	2.4 μm	Transverse resolution	2.4 μm

2.1. Data acquisition and processing

OCT-PAM data acquisition, galvanometer mirrors and the PAM excitation laser are controlled and synchronized with a field-programmable gate array (PCI-7830R, National Instruments). OCT data is captured via a frame grabber (PCIe-1433, National Instruments). Every A-scan is triggered via the frame grabber's real-time system integration bus. Standard OCT data processing (re-scaling, zero padding, dispersion compensation, fast Fourier transform) is performed on the acquired interferograms [36]. Amplitude and phase of each A-scan are extracted.

For DOCT processing, the phase difference between corresponding depth pixels of consecutive A-scans is calculated [37,38]. Quantitative DOCT is verified using constant flow (MGVG Combimat 2000) of a 1:2 mixture of milk diluted with water in a glass capillary [39]. All DOCT images are acquired with 8 kHz line rate and 800 A-scans per B-scan, corresponding to a 10 Hz B-scan frequency. For longitudinal arterial pulse velocity measurements, consecutive single DOCT B-scans are evaluated. To measure the mean absolute velocity, the flow and the vessel diameter, ten consecutive DOCT B-scans are averaged in complex space to cover two full heartbeats of the zebrafish embryo [40]. This measurement is repeated five times to evaluate the repeatability of the DOCT evaluation. The vessel geometry is extracted from the 3-D image. The vessel diameter d is calculated by averaging the values retrieved from vessel geometry and axial d_{axial} as well as transverse vessel diameter d_{trans} (Fig. 1(b)). The axial velocity v_{axial} is then extracted from the phase difference image [37,38] and the absolute velocity v and mean blood flow F are calculated with Doppler angle (α) compensation (Eq. (1)).

$$v = \frac{v_{axial}}{\cos(\alpha)} \text{ and } F = v \frac{\pi d^2}{4} \quad (1)$$

For PAM, the pump laser is set to always lase in order to avoid uncontrolled and too high pulse energies for the first few pulses after cavity unload. The dye laser's laser line filter is controlled via software (Thorlabs Kinesis) with a homemade calibrated motorized rotational stage and an actuator (Z218B, Thorlabs) dc servo controller combination (TDC001, Thorlabs) to select the wavelength of interest. Excitation pulse energies are recorded using an energy meter (EnergyMax-USB J-10SI-HE, Coherent) and the output wavelength is monitored by a spectrometer (AVS-USB2000, Avantes). During measurements, a control unit (Eta L Hydrophone, XARION) continuously probes the aknetic sensor to measure the photoacoustic pressure wave [28,29]. Automatic bias tracking adjusts the interrogation wavelength in real time to counteract changes in the ambient environment. The data is acquired with a high-speed data acquisition card (ATS 660, Alazartech). Averaging is performed in a volumetrically normalized way, taking pulse energy variations recorded by the energy meter into consideration.

The least square method (LLS) is used for oxygen saturation (sO_2) calculation [41]. Considering deoxy- and oxyhemoglobin as the only absorbers, the reconstructed PAM image $P(\lambda_i, x, y)$ at a specific wavelength λ_i is given by

$$P(\lambda_i, x, y) = \Phi(\lambda)(\epsilon_{HbR}(\lambda_i)C_{HbR}(x, y) + \epsilon_{HbO_2}(\lambda_i)C_{HbO_2}(x, y)), \quad (2)$$

where $\Phi(\lambda)$, ϵ_{HbR} and ϵ_{HbO_2} denote the local optical fluence and the molar extinction coefficients ($\text{cm}^{-1}\text{M}^{-1}$) of HbR and HbO₂. $C_{HbR}(x, y)$ and $C_{HbO_2}(x, y)$ are the molar concentrations of HbR and HbO₂. After fluence normalization with the calibrated energy meter, $C_{HbR}(x, y)$ and $C_{HbO_2}(x, y)$ can be estimated by illuminating the sample with at least two excitation wavelengths and by solving a set of linear equations [41]. The oxygen saturation for each pixel can then be calculated following Eq. (3).

$$sO_2(x, y) = \frac{C_{HbO_2}(x, y)}{C_{HbO_2}(x, y) + C_{HbR}(x, y)} \cdot 100\% \quad (3)$$

LLS requires the same local optical fluence at different wavelengths after excitation laser energy normalization [42]. This requirement is satisfied for superficial penetration depths as is the case in zebrafish larvae [43].

2.2. Optical blood absorption in zebrafish

Like avian and reptilian erythrocytes, zebrafish erythrocytes are elliptical (typically $7\ \mu\text{m} \cdot 10\ \mu\text{m}$) and nucleated [32,44] in contrast to the disc-shaped (discocyte) red blood cells in healthy mammals. Mammalian erythroid cells undergo enucleation, an asymmetric cell division involving extrusion of a pyknotic nucleus enveloped by the plasma membrane. Mammalian red blood cells do not normally contain a nucleus and are unable to proliferate [45]. In addition, human and zebrafish red blood cells contain different combinations of globin molecules [46,47].

Therefore, it is important to know whether major differences exist for blood absorption in order to accurately quantify the oxygenation levels in the zebrafish vasculature, especially because PAM commonly uses human absorption coefficients for oxygen level extraction in animal models. Since there is no reference on zebrafish blood absorption in the literature, we quantified the zebrafish's optical blood absorption by measuring 5 μL fresh adult zebrafish blood of five specimen using a spectrophotometer (U-2000, Hitachi) at various wavelengths. We mixed the zebrafish blood with 4 mL, 100 % oxygen saturated phosphate buffer at a pH of 7.3 to prepare for the HbO₂ measurement and with 4 mL, 0 % oxygen saturated phosphate buffer at a pH of 7.3 for the Hb measurement. Oxygen-free conditions were achieved by adding sodium dithionite to the solution [48]. Measurements were performed immediately after mixing.

Normalized hemoglobin optical absorption coefficients for human and adult zebrafish blood in the wavelength range of 562 nm to 578 nm can be found in Fig. 2. The red (HbO₂) and blue (Hb) dotted curves visualize zebrafish blood absorption, whereas the solid colored lines indicate human blood absorption. Both human and zebrafish blood absorption curves were used for photoacoustic sO_2 extraction to compare the results with each other. Human hemoglobin absorption coefficients were taken from Scott Prael's web database, who has reviewed and collected spectra to produce an ideal hemoglobin curve [49]. All zebrafish experiments were carried out under anesthesia (150 mg/L tricaine for 5 minutes) followed by euthanasia and were approved by the local ethics committee of the University of Innsbruck.

2.3. Animal preparation

In this study we use larvae of the poorly pigmented zebrafish double mutant *ednrb1a*^{-/-}, *mitfa*^{-/-}. After spawning, eggs are maintained in E3 medium at 28 °C under standard conditions. To

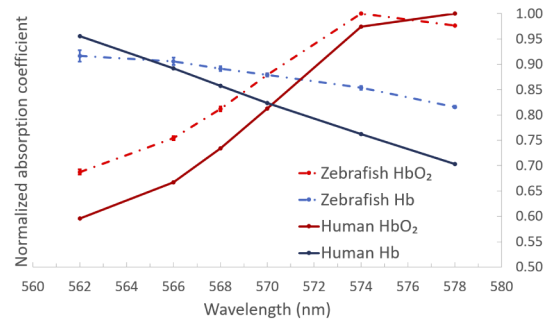


Fig. 2. Normalized hemoglobin absorption coefficients for human and adult zebrafish blood.

further suppress pigmentation, 1-phenyl 2-thiourea (PTU) is added to the medium at 22 - 24 hours post fertilization (hpf). Zebrafish larvae aging 96 - 120 hpf are used for imaging.

2.4. Sample preparation

Zebrafish larvae are anesthetized in 100 mg/L tricaine for 5 minutes. After resting time, the larvae are transferred into a pipette together with 50 μ L of tricaine and 100 μ L of liquid (at 32 °C) 1.5% ultra-low gelling temperature agarose (CAS Number 9012-36-6, Sigma Aldrich). The volume containing the zebrafish is then released into the indentation of a 3-D printed zebrafish mount shown in Fig. 1(c). Under a microscope, a larva can be gently positioned in a recovery position (Fig. 1(d)).

After solidification of the agarose, the fish holder is slid into an adapter plate which is mounted on a three axis manual stage at the position of the “Sample” in Fig. 1 to ensure correct sample placement during imaging. Ultrasound gel (Litho Clear, NEXT Medical Products) is then placed on top of the gelified agarose as acoustic couplant. The aknetic sensor is finally placed and fixed on top and in close proximity to the zebrafish larva (roughly 1 mm) to enable reflection mode OCT-PAM imaging.

3. Results

Figure 3 depicts typical depth sectioned average intensity *en face* projection OCT images of a 5 dpf zebrafish larva acquired with our OCT-PAM system. *En face* projections are averaged every 120 μ m. Several different brain regions can be identified in Fig. 3(a). Going deeper, the ear with two otoliths and melanin structures can be identified (3(b)). The most important landmark in Fig. 3(c) is the zebrafish heart, whose ventricle and atrium are easily identifiable. Figure 3(d) cuts the fish half way through its body, where most morphological features can be found. Apart from pigment cells (ochre), yolk sac (blue square) and swim bladder, the spinal cord (green) and fine structures as well as the zebrafish larva’s internal organs (brown), somites (blue arrow) and the pineal gland are visualized [50]. The notochord (magenta) is visible in Fig. 3(a), (b) and (e).

Figure 4(a) shows an *en face* projection of the larva averaging all sagittal slices. In addition to the morphological contrast based on light scattering provided by OCT, PAM adds a contrast channel based on absorption. Correspondingly, Fig. 4(b) illustrates the averaged (25x) maximum amplitude projection PAM image of the zebrafish larva. While OCT reveals tissue structures, blood vessels such as the dorsal aorta (DA), the caudal vein (CV), the dorsal longitudinal anastomotic vessel (DLAV) and the intersegmental vessels (ISV) are visualized in the PAM image. Due to melanin absorption in the pigmented retina, the eyes of the larva show the strongest signals. It is worth noting that the swim bladder (SB) is visible due to negative contrast, since no absorbers are present within the swim bladder. The image channels of OCT and PAM can be

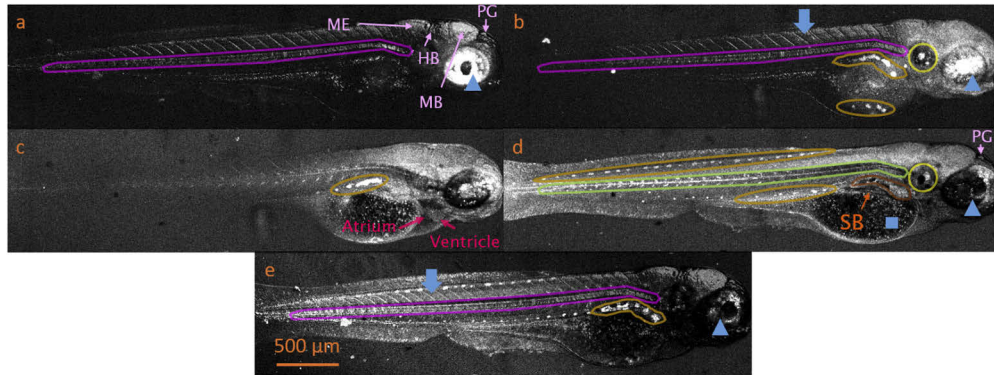


Fig. 3. Depth sectioned OCT average intensity *en face* projections (slab size 120 μm). The uppermost slice starts with the focus at the position of the eye (a) continuing depth increments through the body (b)-(d) to the tail in (e), spanning a total depth of 600 μm . Blue triangle: eye; blue square: yolk sac; blue arrow: myotomes; ochre: pigment cells; yellow: ear with two otoliths; magenta: notochord; green: spinal cord; brown: internal organs; ME: Myelencephalon; HB: hindbrain; MB: midbrain; PG: pineal gland; SB: swim bladder.

overlaid without further processing (Fig. 4(c)) thanks to the inherently co-registered imaging scheme.

Figure 5(a) depicts a cross-sectional OCT B-scan at the position of the dotted vertical line in Fig. 4(a). Several morphological features such as the notochord (magenta), spinal cord (green), lateral line (yellow) and the myotomes (blue arrows) are readily identifiable on the cross-section level. These morphological features can be confirmed in the histology section shown in Fig. 5(b), which is acquired from a similar fish at 5 dpf.

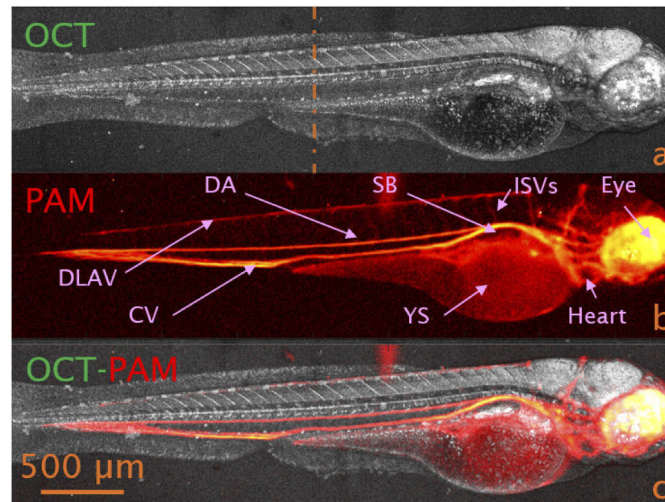


Fig. 4. OCT-PAM image of a zebrafish larva. (a) OCT average intensity projection, (b) PAM maximum amplitude projection, (c) multimodal OCT-PAM. The 50 kHz 532 nm pump laser was used to acquire the PAM image. DA: dorsal aorta; CV: caudal vein; DLAV: dorsal longitudinal anastomotic vessel; SB: swim bladder; YS: yolk sac; ISV: intersegmental vessel.

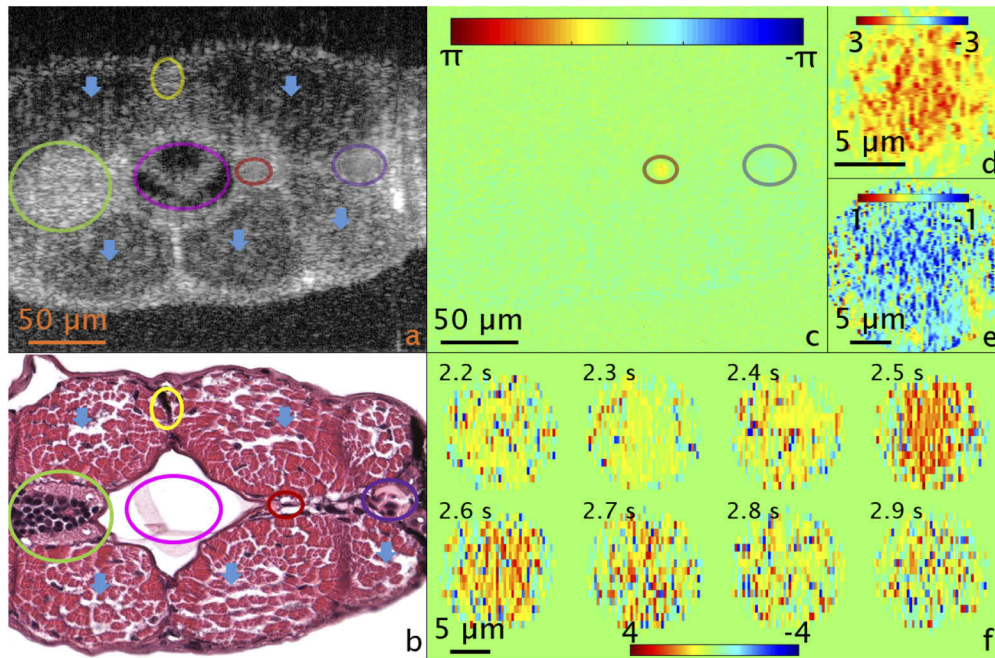


Fig. 5. Comparison between OCT, DOCT and histology. (a) OCT B-scan at the position of the brown vertical line in Fig. 4(a). (b) Histology, transverse image from a 5 dpf zebrafish larva at a similar anterior-posterior position [51]. (c) Phase difference image from a. Color bar indicates phase in rad. (d) Velocity profile of the DA, (e) CV, and (f) velocity profiles of the DA at different timepoints after Doppler angle correction. Color bar indicates velocity in mm/s. Magenta ellipse: notochord; green ellipse: spinal cord; yellow ellipse: lateral line; red ellipse: dorsal aorta; purple ellipse: caudal vein; blue arrows: myotomes (segmental muscles).

Because moving red blood cells create a different speckle pattern compared to static tissue in an averaged B-scan, the DA (red ellipse) and CV (purple ellipse), marked in Fig. 5(a), can be identified by searching for this pattern.

The corresponding DOCT image (Fig. 5(c)) immediately reveals the location of those vessels since the DA appears in yellow color (positive phase difference and blood movement direction) and the CV in blue color (negative phase difference and blood movement direction), while static tissue appears in green color. Figure 5(d) and (e) show the respective absolute velocity profiles at the zoomed in position of the two vessels. Figure 5(f) depicts absolute velocity profiles in the DA for different time points within one cardiac cycle between second 2.2 and 2.9 of the 3 s imaging interval. Five cardiac cycles are recorded within the 3 s imaging window, corresponding to a heart rate of 120 beats per minute. The DOCT evaluation for all time points is depicted in Fig. 6. All velocity profiles are calculated with Doppler angle compensation (Eq. (1)). Table 2 presents quantitative DOCT results for the DA and CV. Five independent DOCT evaluations are performed at the same position of the zebrafish larva to calculate mean and standard deviation. Table 2 also summarizes longitudinal DA quantitative DOCT results for five cardiac cycles.

The fine structures of the zebrafish larva's retina are revealed by ultra-high resolution OCT in the right image of Fig. 7. Different intensity contrast can be found for different retinal layers in the cross-sectional OCT image indicating the position and thickness of these layers. The ganglion cell layer (1), inner plexiform layer (2), inner nuclear layer (3), outer nuclear layer (4) and retinal pigmented epithelium (green ellipse) can be visualized and identified. The outer

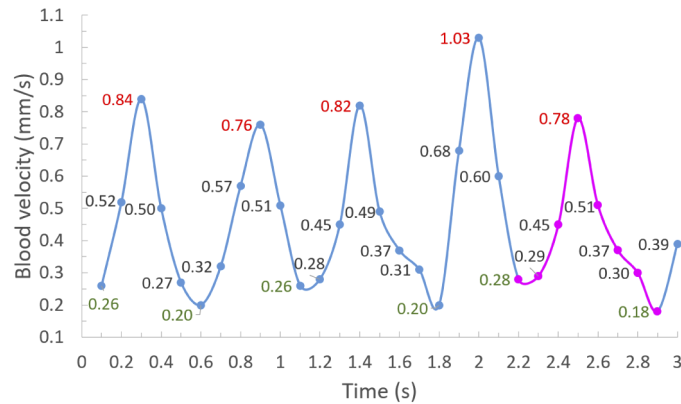


Fig. 6. Longitudinal DOCT blood velocity evaluation in the DA. 10 Hz sample frequency, 30 samples. red values: local peak velocities, green values: local minimum velocities, magenta curve section: velocity evaluation for the data illustrated in Fig. 5(f).

Table 2. Quantitative DOCT evaluation.

	Vessel diameter	Mean velocity	Mean flow
DA	$12.8 \pm 0.5 \mu\text{m}$	$544 \pm 40 \mu\text{m/s}$	$4.21 \pm 0.63 \text{ nL/min}$
CV	$23.3 \pm 1.4 \mu\text{m}$	$165 \pm 12 \mu\text{m/s}$	$4.23 \pm 0.81 \text{ nL/min}$
HYA	$18.1 \pm 1.9 \mu\text{m}$	$210 \pm 60 \mu\text{m/s}$	$3.2 \pm 1.6 \text{ nL/min}$
	Peak velocity	Minimum velocity	Overall velocity
DA	$846 \pm 108 \mu\text{m/s}$	$230 \pm 41 \mu\text{m/s}$	$460 \pm 220 \mu\text{m/s}$

plexiform layer cannot be visualized throughout the whole B-scan but is resolvable in some parts of the image (green arrow). The OCT B-scan is compared with histology results (Fig. 7, left), which depict a transverse section cut through the center of a similar 5 dpf zebrafish larval eye. The hyaloid artery (HYA, blue triangle), which supplies blood to the retina of the zebrafish at this age, is clearly visualized in the DOCT overlay in Fig. 7. We measured the mean diameter of the HYA and the absolute velocity and flow rate of blood within the artery of five 5 dpf zebrafish

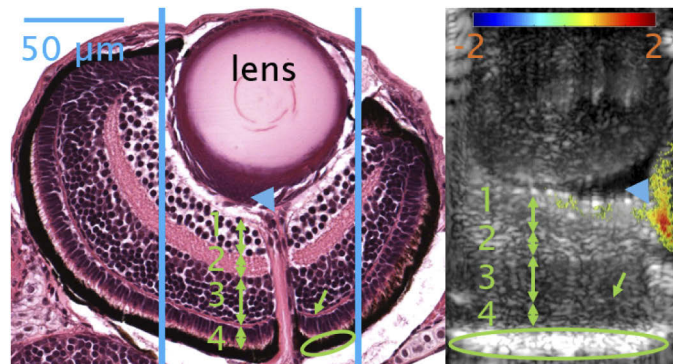


Fig. 7. Histology [52] and DOCT side by side comparison (transverse cut). Blue bars: region of interest for OCT imaging; green arrows: retinal layers; 1: ganglion cell layer; 2: inner plexiform layer; 3: inner nuclear layer; 4: outer nuclear layer; green ellipse: retinal pigmented epithelium; blue triangle: HYA. Color bar for phase difference overlay: $\pm 2 \text{ rad}$.

larvae using the absolute velocity extraction principle (Fig. 1(b) and Eq. (1)). The results are summarized in Table 2.

To provide *in vivo* oxygenation measurements, three PAM maximum amplitude projection images are acquired with the dye laser at a repetition rate of 10 kHz. The wavelengths 578 nm, 570 nm and 562 nm are selected for this measurement. 578 nm and 562 nm are used for the high absorption coefficients of oxygenated blood and deoxygenated blood, respectively. The corresponding isosbestic point in the selectable wavelength region of the dye laser corresponds to 570 nm.

Figure 8(a) illustrates the oxygen saturation map using the human absorption coefficients, while the lower map presents the respective oxygen saturation map using the absorption coefficients for adult zebrafish blood from Fig. 2. The average sO_2 in the DA is calculated to be $75 \pm 16\%$ and $58 \pm 25\%$ in the CV. The values for the zebrafish absorption coefficients are found to be $76 \pm 16\%$ and $57 \pm 22\%$.

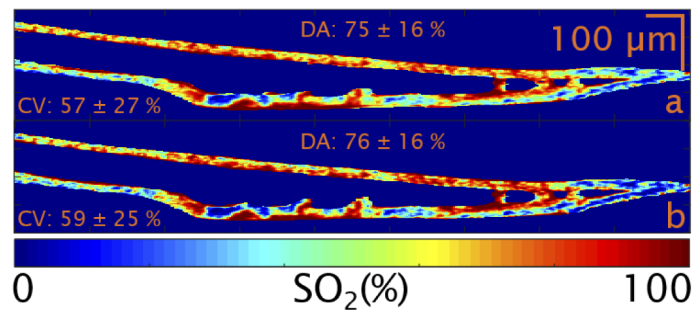


Fig. 8. Oxygenation map of a zebrafish larval tail. The image is acquired after spectral unmixing using the absorption coefficients of human (a) and zebrafish blood (b), respectively.

4. Discussion

Most PAM systems used for zebrafish larval imaging employ a focused ultrasound transducer as photoacoustic detector [15,16,24,25]. In this case the acoustic focus needs to be carefully aligned to overlap with the optical focus of the excitation laser. This requirement necessitates the use of a transmission mode system with a water tank. To generate a volumetric image, the laser beam and the transducer need to be mechanically scanned at the same time, leading to imaging sessions of several dozen minutes to hours [15,16,24–26]. The transmission working mode also limits the integration of other imaging modalities. These limitations are circumvented in our system using the akinetic sensor featuring a large optically transparent window. The excitation laser can now pass through the optical window and PAM can easily be operated in reflection mode. The use of scanning mirrors instead of mechanical stages nor voice coils makes the imaging time of our system only limited to the repetition rate of the excitation laser. The total image acquisition time for a whole zebrafish larva with approximate dimensions of $4\text{ mm} \cdot 0.5\text{ mm}$ and a step size of $1.25\ \mu\text{m}$ is 25.6 s without averaging. The PAM image of the zebrafish larva in Fig. 4(b) is acquired in approximately ten minutes, since 25 averages are necessary to image the intersegmental vessels. When only the DA and CV are of interest, five times averaging or two minutes suffice to image the whole zebrafish larva. It takes approximately 4 minutes and 30 seconds acquiring $1400 \cdot 400$ pixels with a step size of $1.25\ \mu\text{m}$ using the 10 kHz dye laser to record a single wavelength image, resulting in a total imaging time of 13 minutes and 30 seconds to reconstruct the oxygen maps in Fig. 8. With emerging supercontinuum lasers running at MHz range for PAM [53], even shorter imaging time can be achieved.

Detailed oxygen maps for zebrafish larvae as well as zebrafish blood absorption coefficients have not been reported before, therefore it is hard to compare the measured oxygen saturation in the DA and CV to previous results. [54] investigated oxygen saturation of the blood in the ventricle of normoxic zebrafish larvae *in vivo* by incubating the larva in a tiny chamber between polytetrafluoroethylene membranes with the possibility to change the oxygenation saturation rapidly. Oxygen saturation levels were measured in the ventricle of the zebrafish heart by combining video imaging techniques with a spectrophotometrical analysis of hemoglobin light absorption at specific wavelengths namely 413 nm and 431 nm. An oxygen saturation of approximately $78 \pm 2\%$ in the larva's ventricle at the age of 5 dpf was reported [54]. This value corresponds well to the average value of 76% oxygen saturation in the DA of 5 dpf zebrafish larvae measured with our sPAM setup. The standard deviation is not comparable, since [54] describe average oxygenation measured for several zebrafish larvae, while OCT-PAM allows to study variations on a microscopic level, which is not achievable with other imaging technologies.

The oxygen saturation in the zebrafish larva seems to be non-uniform with higher variation in the CV (Fig. 8). Since the oxygen maps were generated by imaging the zebrafish larva for 13 minutes, such behavior might be explained by different resting times and flow velocities of individual erythrocytes within the CV. [55] reported different erythrocyte counts per minute at different locations within both major blood vessels by investigating the blood distribution using digital motion analysis [55]. The variation of the red blood cell count was higher for the CV, especially in the tail region. A mathematical model for the behavior of red blood cells within the CV of 36 hpf zebrafish larvae also suggests a highly non-uniform flow distribution [56], which supports our findings. To better understand the presented behavior, decreased oxygen map acquisition times with new laser technologies and imaging of smaller field of views might give information on the real time oxygen saturation of individual blood cells, which can be tracked over time in the future [57].

OCT imaging of zebrafish larvae has been reported before [58–60]. Previously, lower bandwidth OCT sources were used, limiting the axial resolution of the respective systems. We present an ultra-high resolution OCT system with an axial resolution of $2.4 \mu\text{m}$ in tissue. The acquired images compare well to histology and most morphological landmarks can be clearly identified. In addition, we were able to resolve most retinal layers in the larval eye *in vivo* in an OCT B-scan, which has not been reported before. We believe OCT can provide a significant advantage by mapping the 3-D structure of the zebrafish larva, since basically every organ, the notochord, spinal cord, the individual heart chambers, the eye and the brain can be visualized and their volume can be quantified *in vivo*.

We visualized and quantified blood flow and velocity in the DA and the CV of the body as well as in the HYA in the zebrafish by DOCT. DOCT was used to measure peak blood velocity in the ventral aorta by a dual beam OCT system before [61], but there are no comparable results for the DA, CV and HYA. [62] reported mean flow velocities of $527 \pm 39 \mu\text{m/s}$ with average peak and minimum aortic flow velocities of $846 \pm 80 \mu\text{m/s}$ and $209 \pm 14 \mu\text{m/s}$ averaged over several heart cycles for 5 dpf zebrafish larvae using a high-speed complementary metal-oxide-semiconductor camera with a framerate of 486 frames per second [62]. Our reported values for average mean ($544 \pm 40 \mu\text{m/s}$), peak and minimum aortic velocities ($846 \pm 108 \mu\text{m/s}$ and $230 \pm 41 \mu\text{m/s}$) correspond well to the reported values. Blood flow rate measurements in the CV have not been reported elsewhere. DOCT with Doppler angle compensation offers a critical advantage over current technologies, since it does not depend on the geometry of the vasculature and is even more sensitive to blood flow in the axial direction. Classical approaches as in [62] require a flat geometry (preferably 2-D) to accurately detect flow velocities and will underestimate flow velocities, should there be an angle between the vascular layer and the imaging plane.

The HYA is only accessible through the eye's lens, where the artery is positioned nearly parallel to the optical axis. Because of the previously mentioned advantages, DOCT is the

only imaging modality which allows to quantify the flow velocities in those situations, since traditional methods will not see any flow. The availability of several disease models for zebrafish larvae including eye and retinal diseases with potential, but yet unknown impact on vascular aspects, show that DOCT is a very powerful tool to answer critical medical questions concerning the pathophysiology of highly prevalent and severe eye diseases such as glaucomatous optic neuropathy and age related macular degeneration [5,33].

5. Conclusion

We present a fast scanning multimodal OCT-PAM system to image both the scattering and absorption contrast of zebrafish larvae. In addition to the basic contrast mechanisms we demonstrate that ultra-high resolution OCT is capable to resolve retinal layers *in vivo* in a zebrafish larva in B-scan mode and that DOCT allows to study retinal blood supply by investigating the HYA. DOCT is also applied to other parts of the zebrafish larva, where we are able to measure time variations in the aortic flow, mean absolute blood velocity and flow rate. sPAM is used to reconstruct oxygen saturation levels in the DA and CV, showing regional differences of oxygen distribution and oxygen transfer from the DA to the CV. Our work clearly demonstrates the significance of OCT and PAM applied in zebrafish, since a multimodal system with functional extensions can give unprecedented insight into morphology and physiological processes of this animal model. We envision that our novel non-invasive and label-free imaging modality in combination with zebrafish will enable an improved understanding of cardiovascular development. Furthermore, as several models for cardiovascular diseases are available in zebrafish, our imaging setup will also contribute to a more detailed characterization of the respective pathology and its underlying molecular mechanisms. In addition, the effect of drug candidates can be studied *in vivo* to ultimately provide novel therapeutic strategies.

Funding

Österreichische Forschungsförderungsgesellschaft (5035366, 855797); H2020 LEIT Information and Communication Technologies (732720); FP7 Information and Communication Technologies (317744).

Acknowledgments

We thank Keith Oakes in Elforlight for servicing the PAM excitation source. Ewald Unger for helping with the design and 3-D printing of various phantoms and zebrafish mounts and Martin Stoiber and Christian Grasl for general support concerning tubings and plastic parts.

We acknowledge <http://zfatlas.psu.edu/>, NIH grant 5R24 RR01744, Jake Gittlen Cancer Research Foundation and PA Tobacco Settlement Fund for providing free access and usage of zebrafish larva histology images.

Disclosures

Wolfgang Rohringer: XARION Laser Acoustics GmbH (FEP), Balthasar Fischer: XARION Laser Acoustics GmbH (FIP). The authors declare no conflicts of interest.

References

1. H. W. Detrich, M. Westerfield, and L. I. Zon, "Overview of the Zebrafish system," *Methods Cell Biol.* **59**, 3–10 (1998).
2. G. Streisinger, C. Walker, N. Dower, D. Knauber, and F. Singer, "Production of clones of homozygous diploid zebra fish (*Brachydanio rerio*)," *Nature* **291**(5813), 293–296 (1981).
3. B. Pelster and W. W. Burggren, "Disruption of hemoglobin oxygen transport does not impact oxygen-dependent physiological processes in developing embryos of zebra fish (*Danio rerio*)," *Circ. Res.* **79**(2), 358–362 (1996).

4. S. Isogai, M. Horiguchi, and B. M. Weinstein, "The Vascular Anatomy of the Developing Zebrafish: An Atlas of Embryonic and Early Larval Development," *Dev. Biol. (Amsterdam, Neth.)* **230**(2), 278–301 (2001).
5. G. Kari, U. Rodeck, and A. P. Dicker, "Zebrafish: An Emerging Model System for Human Disease and Drug Discovery," *Clin. Pharmacol. Ther. (Hoboken, NJ, U. S.)* **82**(1), 70–80 (2007).
6. A. L. Rubinstein, "Zebrafish assays for drug toxicity screening," *Expert Opin. Drug Metab. Toxicol.* **2**(2), 231–240 (2006).
7. B. M. Weinstein, D. L. Stemple, W. Driever, and M. C. Fishman, "gridlock, a localized heritable vascular patterning defect in the zebrafish," *Nat. Med.* **1**(11), 1143–1147 (1995).
8. S. Rieger, R. P. Kulkarni, D. Darcy, S. E. Fraser, and R. W. Köster, "Quantum dots are powerful multipurpose vital labeling agents in zebrafish embryos," *Dev. Dyn.* **234**(3), 670–681 (2005).
9. D. Baldessari and M. Mione, "How to create the vascular tree? (Latest) help from the zebrafish," *Pharmacol. Ther.* **118**(2), 206–230 (2008).
10. B. L. Roman and B. M. Weinstein, "Building the vertebrate vasculature: research is going swimmingly," *BioEssays* **22**(10), 882–893 (2000).
11. K. Wada, T. Masujima, H. Yoshida, T. Murakami, N. Yata, and H. Imai, "Application of Photoacoustic Microscopy to Analysis of Biological Components in Tissue Sections," *Chem. Pharm. Bull.* **34**(4), 1688–1693 (1986).
12. S. Manohar and D. Razansky, "Photoacoustics: a historical review," *Adv. Opt. Photonics* **8**(4), 586–617 (2016).
13. D. Huang, E. A. Swanson, C. P. Lin, J. S. Schuman, W. G. Stinson, W. Chang, M. R. Hee, T. Flotte, K. Gregory, C. A. Puliafito, and J. G. Fujimoto, "Optical coherence tomography," (1991).
14. A. Fercher, C. Hitzenberger, and M. Juchem, "Measurement of Intraocular Optical Distances Using Partially Coherent Laser Light," *J. Mod. Opt.* **38**(7), 1327–1333 (1991).
15. S. Ye, R. Yang, J. Xiong, K. K. Shung, Q. Zhou, C. Li, and Q. Ren, "Label-free imaging of zebrafish larvae in vivo by photoacoustic microscopy," *Biomed. Opt. Express* **3**(2), 360–365 (2012).
16. Q. Chen, T. Jin, W. Qi, X. Mo, and L. Xi, "Label-free photoacoustic imaging of the cardio-cerebrovascular development in the embryonic zebrafish," *Biomed. Opt. Express* **8**(4), 2359–2367 (2017).
17. X. Zhang, H. F. Zhang, and S. Jiao, "Optical coherence photoacoustic microscopy: accomplishing optical coherence tomography and photoacoustic microscopy with a single light source," *J. Biomed. Opt.* **17**(3), 030502 (2012).
18. X. Liu, T. Liu, R. Wen, Y. Li, C. A. Puliafito, H. F. Zhang, and S. Jiao, "Optical coherence photoacoustic microscopy for in vivo multimodal retinal imaging," *Opt. Lett.* **40**(7), 1370–1373 (2015).
19. Z. Chen, S. Yang, Y. Wang, and D. Xing, "All-optically integrated photo-acoustic microscopy and optical coherence tomography based on a single Michelson detector," *Opt. Lett.* **40**(12), 2838–2841 (2015).
20. Z. Chen, S. Yang, and D. Xing, "Optically integrated trimodality imaging system: combined all-optical photoacoustic microscopy, optical coherence tomography, and fluorescence imaging," *Opt. Lett.* **41**(7), 1636–1639 (2016).
21. W. Zhang, Y. Li, V. P. Nguyen, Z. Huang, Z. Liu, X. Wang, and Y. M. Paulus, "High-resolution, in vivo multimodal photoacoustic microscopy, optical coherence tomography, and fluorescence microscopy imaging of rabbit retinal neovascularization," *Light: Sci. Appl.* **7**(1), 103 (2018).
22. W. Song, Q. Wei, W. Liu, T. Liu, J. Yi, N. Sheibani, A. A. Fawzi, R. A. Linsenmeier, S. Jiao, and H. F. Zhang, "A combined method to quantify the retinal metabolic rate of oxygen using photoacoustic ophthalmoscopy and optical coherence tomography," *Sci. Rep.* **4**(1), 6525 (2015).
23. B. Rao, F. Soto, D. Kerschensteiner, and L. V. Wang, "Integrated photoacoustic, confocal, and two-photon microscope," *J. Biomed. Opt.* **19**(3), 036002 (2014).
24. D. Soliman, G. J. Tservelakis, M. Omar, and V. Ntziachristos, "Combining microscopy with mesoscopy using optical and optoacoustic label-free modes," *Sci. Rep.* **5**(1), 12902 (2015).
25. M. J. Moore, S. El-Rass, Y. Xiao, Y. Wang, X.-Y. Wen, and M. C. Kolios, "Simultaneous ultra-high frequency photoacoustic microscopy and photoacoustic radiometry of zebrafish larvae in vivo," *Photoacoustics* **12**, 14–21 (2018).
26. M. J. Moore, E. M. Strohm, and M. C. Kolios, "Triplex micron-resolution acoustic, photoacoustic, and optical transmission microscopy via photoacoustic radiometry," *Opt. Express* **26**(17), 22315–22326 (2018).
27. C. Liu, J. Liao, L. Chen, J. Chen, R. Ding, X. Gong, C. Cui, Z. Pang, W. Zheng, and L. Song, "The integrated high-resolution reflection-mode photoacoustic and fluorescence confocal microscopy," *Photoacoustics* **14**, 12–18 (2019).
28. R. Haindl, S. Preisser, M. Andreana, W. Rohringer, C. Sturtzel, M. Distel, Z. Chen, E. Rank, B. Fischer, W. Drexler, and M. Liu, "Dual modality reflection mode optical coherence and photoacoustic microscopy using an akinetic sensor," *Opt. Lett.* **42**(21), 4319–4322 (2017).
29. S. Preisser, W. Rohringer, M. Liu, C. Kollmann, S. Zotter, B. Fischer, and W. Drexler, "All-optical highly sensitive akinetic sensor for ultrasound detection and photoacoustic imaging," *Biomed. Opt. Express* **7**(10), 4171–4186 (2016).
30. S. Jiao and M. Ruggeri, "Polarization effect on the depth resolution of optical coherence tomography," *J. Biomed. Opt.* **13**(6), 060503 (2008).
31. G. Follain, N. Osmani, A. S. Azevedo, G. Allio, L. Mercier, M. A. Karreman, G. Solecki, M. J. Garcia Leòn, O. Lefebvre, N. Fekonja, C. Hille, V. Chabannes, G. Dollé, T. Metivet, F. D. Hovsepian, C. Prudhomme, A. Pichot, N. Paul, R. Carapito, S. Bahram, B. Ruthensteiner, A. Kemmling, S. Siemonsen, T. Schneider, J. Fiehler, M. Glatzel, F. Winkler, Y. Schwab, K. Pantel, S. Harlepp, and J. G. Goetz, "Hemodynamic Forces Tune the Arrest, Adhesion, and Extravasation of Circulating Tumor Cells," *Dev. Cell* **45**(1), 33–52.e12 (2018).

32. D. Carradice and G. J. Lieschke, "Zebrafish in hematology: sushi or science?" *Blood* **111**(7), 3331–3342 (2008).
33. J. Chhetri, G. Jacobson, and N. Gueven, "Zebrafish—on the move towards ophthalmological research," *Eye* **28**(4), 367–380 (2014).
34. S. S. Kitambi, K. J. McCulloch, R. T. Peterson, and J. J. Malicki, "Small molecule screen for compounds that affect vascular development in the zebrafish retina," *Mech. Dev.* **126**(5-6), 464–477 (2009).
35. G. Gestri, B. A. Link, and S. C. F. Neuhauss, "The visual system of zebrafish and its use to model human ocular diseases," *Dev. Neurobiol.* **72**(3), 302–327 (2012).
36. R. Haindl, W. Trasischker, A. Wartak, B. Baumann, M. Pircher, and C. K. Hitzenberger, "Total retinal blood flow measurement by three beam Doppler optical coherence tomography," *Biomed. Opt. Express* **7**(2), 287–301 (2016).
37. X. J. Wang, T. E. Milner, and J. S. Nelson, "Characterization of fluid flow velocity by optical Doppler tomography," *Opt. Lett.* **20**(11), 1337–1339 (1995).
38. Z. Chen, T. E. Milner, D. Dave, and J. S. Nelson, "Optical Doppler tomographic imaging of fluid flow velocity in highly scattering media," *Opt. Lett.* **22**(1), 64–66 (1997).
39. R. Haindl, W. Trasischker, B. Baumann, M. Pircher, and C. K. Hitzenberger, "Three-beam Doppler optical coherence tomography using a facet prism telescope and MEMS mirror for improved transversal resolution," *J. Mod. Opt.* **62**(21), 1781–1788 (2015).
40. A. Szkulmowska, M. Szkulmowski, A. Kowalczyk, and M. Wojtkowski, "Phase-resolved Doppler optical coherence tomography—limitations and improvements," *Opt. Lett.* **33**(13), 1425–1427 (2008).
41. M. Li, Y. Tang, and J. Yao, "Photoacoustic tomography of blood oxygenation: A mini review," *Photoacoustics* **10**, 65–73 (2018).
42. S. Kim, Y.-S. Chen, G. P. Luke, and S. Y. Emelianov, "In vivo three-dimensional spectroscopic photoacoustic imaging for monitoring nanoparticle delivery," *Biomed. Opt. Express* **2**(9), 2540–2550 (2011).
43. E. W. Stein, K. Maslov, and L. V. Wang, "Noninvasive, in vivo imaging of blood-oxygenation dynamics within the mouse brain using photoacoustic microscopy," *J. Biomed. Opt.* **14**(2), 020502 (2009).
44. D. G. Ransom, P. Haffter, J. Odenthal, A. Brownlie, E. Vogelsang, R. N. Kelsch, M. Brand, F. J. van Eeden, M. Furutani-Seiki, M. Granato, M. Hammerschmidt, C. P. Heisenberg, Y. J. Jiang, D. A. Kane, M. C. Mullins, and C. Nusslein-Volhard, "Characterization of zebrafish mutants with defects in embryonic hematopoiesis," *Development* **123**, 311–319 (1996).
45. A. R. Migliaccio, "Erythroblast enucleation," *Haematologica* **95**(12), 1985–1988 (2010).
46. L. R. Manning, J. E. Russell, J. C. Padovan, B. T. Chait, A. Popowicz, R. S. Manning, and J. M. Manning, "Human embryonic, fetal, and adult hemoglobins have different subunit interface strengths. Correlation with lifespan in the red cell," *Protein Sci.* **16**(8), 1641–1658 (2007).
47. J. J. Ganis, N. Hsia, E. Trompouki, J. L. de Jong, A. DiBiase, J. S. Lambert, Z. Jia, P. J. Sabo, M. Weaver, R. Sandstrom, J. A. Stamatoyannopoulos, Y. Zhou, and L. I. Zon, "Zebrafish globin switching occurs in two developmental stages and is controlled by the LCR," *Dev. Biol. (Amsterdam, Neth.)* **366**(2), 185–194 (2012).
48. H. J. Atkinson, "The functional significance of the haemoglobin in a marine nematode, *Enoplus brevis* (Bastian)," *J. Exp. Biol.* **62**, 1–9 (1975).
49. S. Prah, "Tabulated molar extinction coefficient for hemoglobin in water," <http://omlc.ogi.edu/spectra/hemoglobin/summary.html>.
50. L. Ruzicka, D. Howe, S. Ramachandran, S. Toro, C. Van Slyke, Y. Bradford, A. Eagle, D. Fashena, K. Frazer, P. Kalita, P. Mani, R. Martin, S. Moxon, H. Paddock, C. Pich, K. Schaper, X. Shao, A. Singer, and M. Westerfield, "The Zebrafish Information Network: The new support for non-coding genes, richer Gene Ontology annotations and the Alliance of Genome Resources," *Nucleic Acids Res.* **47**(D1), D867–D873 (2019).
51. zfatlas.psu.edu, "Zebrafish Atlas," <http://bio-atlas.psu.edu/zf/view.php?s=397&atlas=10>.
52. zfatlas.psu.edu, "Zebrafish Atlas," <http://bio-atlas.psu.edu/zf/view.php?s=376&atlas=10>.
53. Y. Chang, Y. Hu, Z. Chen, and D. Xing, "Co-impulse multispectral photoacoustic microscopy and optical coherence tomography system using a single supercontinuum laser," *Opt. Lett.* **44**(18), 4459–4462 (2019).
54. S. Grillitsch, N. Medgyesy, T. Schwerte, and B. Pelster, "The influence of environmental PO₂ on hemoglobin oxygen saturation in developing zebrafish *Danio rerio*," *J. Exp. Biol.* **208**(2), 309–316 (2005).
55. T. Schwerte, D. Uberbacher, and B. Pelster, "Non-invasive imaging of blood cell concentration and blood distribution in zebrafish *Danio rerio* incubated in hypoxic conditions in vivo," *J. Exp. Biol.* **206**(8), 1299–1307 (2003).
56. T. R. Djukic, S. Karthik, I. Saveljic, V. Djonov, and N. Filipovic, "Modeling the Behavior of Red Blood Cells within the Caudal Vein Plexus of Zebrafish," *Front. Physiol.* **7**, 455 (2016).
57. L. Wang, K. Maslov, and L. V. Wang, "Single-cell label-free photoacoustic flowoxigraphy in vivo," *Proc. Natl. Acad. Sci.* **110**(15), 5759–5764 (2013).
58. L. Kagemann, H. Ishikawa, J. Zou, P. Charukamnoetkanok, G. Wollstein, K. A. Townsend, M. L. Gabriele, N. Bahary, X. Wei, J. G. Fujimoto, and J. S. Schuman, "Repeated, noninvasive, high resolution spectral domain optical coherence tomography imaging of zebrafish embryos," *Mol. Vis.* **14**, 2157–2170 (2008).
59. K. Divakar Rao, P. Upadhyaya, M. Sharma, and P. K. Gupta, "Noninvasive Imaging of Ethanol-Induced Developmental Defects in Zebrafish Embryos Using Optical Coherence Tomography," *Birth Defects Res., Part B* **95**(1), 7–11 (2011).
60. K. Pekkan, B. Chang, F. Uslu, K. Mani, C.-Y. Chen, and R. Holzman, "Characterization of zebrafish larvae suction feeding flow using μ PIV and optical coherence tomography," *Exp. Fluids* **57**(7), 112 (2016).

61. N. V. Iftimia, D. X. Hammer, R. D. Ferguson, M. Mujat, D. Vu, and A. A. Ferrante, "Dual-beam Fourier domain optical Doppler tomography of zebrafish," *Opt. Express* **16**(18), 13624–13636 (2008).
62. S. C. Watkins, S. Maniar, M. Mosher, B. L. Roman, M. Tsang, and C. M. S. Croix, "High Resolution Imaging of Vascular Function in Zebrafish," *PLoS One* **7**(8), e44018 (2012).